minerals

Article

A Tiny-Fault Detection Strategy Based on Phase Congruency—An Example of Carbonate Reservoir in Ordos Basin, China

Enli Wang *, Hailiang Li, Run He *, Wanjin Zhao, Lin Li, Chunhui Xie, Guoliang Yan, Qiyan Chen and Qing Yang

Research Institute of Petroleum Exploration & Development-Northwest (NWGI), PetroChina, Lanzhou 730000, China
* Correspondence: wangenli@petrochina.com.cn (E.W.); he_run@petrochina.com.cn (R.H.)

Abstract: Tiny-fault detection plays a very important role in the research on the tight oil and gas reservoir in well area X in Ordos Basin, China. In this study, the target formation is the Majiagou dolomite reservoir section under the Ordovician salt with low-amplitude structures generally developed. The conventional attributes extracted from migrated seismic data could not achieve ideal results in detecting hidden faults with small displacement due to slight travel time differences and weak amplitude disturbances. To address this challenge, a segment and fusion strategy was adopted to highlight tiny faults in this region. First, the phase congruency analysis method was used to extract the local edges of coherence to locate the faults. Second, in the extraction process, the coherence was divided into segments according to the fault scales, and then enhanced segment by segment and fused. Third, the empirical formula of the new fault indicator was constructed by the phase congruency features, which can be used to accurately characterize tiny faults. This strategy performs well in both model tests and the migrated seismic data.

Keywords: tiny faults; amplitude; phase; phase congruency; segment; fusion; strategy

check for updates

Citation: Wang, E.; Li, H.; He, R.; Zhao, W.; Li, L.; Xie, C.; Yan, G.; Chen, Q.; Yang, Q. A Tiny-Fault Detection Strategy Based on Phase Congruency—An Example of Carbonate Reservoir in Ordos Basin, China. *Minerals* **2023**, *13*, 306. https://doi.org/10.3390/min13030306

Academic Editors: Stanisław Mazur, Guoqiang Xue, Nannan Zhou, Weiying Chen and Haiyan Yang

Received: 20 November 2022
Revised: 15 February 2023
Accepted: 18 February 2023
Published: 22 February 2023

1. Introduction

Fractured reservoirs with low porosity and low permeability have been regarded as important remaining hydrocarbon resources [1–5]. In the exploration stage, the distribution of tiny faults, which usually refer to faults with displacement less than 5 m [6–13], is crucial for understanding the reservoir formation, hydrocarbon migration, and gas and oil preservation, and helps the delineation of favorable zones and good deployment. In the development stage, unknown faults may reduce the effectiveness of hydraulic fracturing, such as causing leakage of fracturing fluid, jointing adjacent water layers, damaging shallow aquifers [14,15], and even triggering geological hazards in some areas [16]. The description of faults or fracture system is meaningful to the structural modeling and reservoir simulation. Moreover, fractures are crucial to carbon dioxide (CO_2) capture, utilization, and storage (CCUS) [17]. Therefore, fault detection techniques have always been an important research field in recent decades and are receiving increasing attention. Furthermore, tiny fault detection is a very serious challenge in this field.

The Ordos Basin, located in the central part of the Chinese continent, is a stable multi-rotation cratonic basin formed on a base of Archean and Lower Paleozoic metamorphic rocks. The study area is mainly located in the east of the central paleo-uplift of the Ordos Basin and on the Yishan slope. At the end of Ordovician, under the influence of the Garidonian tectonic movement, the strata of Majiagou Formation near the Central Paleo Uplift suffered different degrees of weathering and denudation, which made the top of Ordovician strata gradually old from east to west. The Ordovician reservoirs in the study area are mainly deposited by marine carbonate rocks. The target formation in well area X is the Majiagou dolomite reservoir section under the Ordovician salt. Low-amplitude structures are generally developed in this area. They are favorable to the local accumulation of natural gas. Faults and fractures in this region are crucial elements to gas exploration. However, most of the faults in the study area are nearly vertical, small-scaled, and lead to slight misalignments of seismic events. Conventional techniques based on amplitude discrepancy, such as coherence [18], variance [19], curvature [20], structure-oriented filtering [21] and so on, could not work well. Geologists and geophysicists agreed that the above techniques were severely limited by small travel time differences and the weak amplitude discrepancy between adjacent seismic traces. How to circumvent the above problems and thus effectively identify tiny faults poses a challenge to geophysicists. In this paper, the phase congruency (*PC*) approach was introduced. A new strategy of segment and fusion process was proposed, and a new fault indicator was constructed. Higher resolution for tiny faults detection was expected to be achieved.

2. Method

Phase congruency (*PC*) analysis is an image feature extraction method. It considers the very points with the most consistent phase of all the Fourier components of an image as the feature points. These points are marked as edges or corners. This method is more reliable than gradient-based ones [22], such as Sobel operator [23], Marr operator [24], Canny operator [25] and so on. Combined with the two-dimensional Log–Gabor filter with multi-scale, multi-azimuth, the 2D *PC* analysis and extraction method was successfully implemented by Kovesi [26–28], which is shown in Appendix A. This method has been applied in seismic interpretation in oil and gas exploration. For example, by applying *PC*, Russell et al. detected vugs and fractures in carbonate reservoirs [29], Shafiq et al. enhanced lava dome features [30], Karbalaali identified channel boundaries [31], Kovesi et al. recognized velocity anomalies and fracture boundaries in seismic data [32], and Liao L. [33] and Wang et al. [34] improved the fault detection resolution.

The classic *PC* analysis methods has two important features. First, the maximum moment M represents tiny edges better, while the amplitude weighted mean local phase angle $\overline{\phi}$ describes edges on a larger scale more reliably. Therefore, a potentially reasonable combination of the two parameters may have the chance of obtaining the best results. Second, the direct application of *PC* was unable to get sufficiently ideal results for fault detection. It was found that two adjacent or intersecting faults with excessive numerical differences will experience significant disturbances [34]. Specifically, in the fault intersection development zone, the primary fault features will be enhanced, while the low-order ones will be severely impaired. If the advantages of *PC* can be fully utilized and the above limitations can be overcome, fault features of higher resolution are likely to be achieved.

For a higher resolution for fault detection, a new strategy of segment extraction and fusion and design for its workflow were proposed. This strategy extracted fault information from the coherence attribute of migrated seismic data by applying the *PC* method. It assumes that coherence in the same value range could present faults of familiar features and will not disturb faults in other ranges. The basic workflow is:

First, coherences of different value ranges were separated. These segments should cover all the coherence values of interest to avoid missing fault features. For convenience, a three-segment division was generally sufficient. Specifically, for the ith time slice of the 3D coherence attributes, three thresholds were set as threshold_1, threshold_2, and threshold_3 and three slices were extracted, named slice_i^1, slice_i^2, and slice_i^3. Then, maximum moment M and the amplitude weighted mean local phase angle $\overline{\phi}$ were extracted.

Secondly, a fusion to balance the uniform background with detailed discontinuities was carried out. This was given by the following new empirical fault indicator F:

$$F = \exp(-\overline{\phi}) \times (\exp(M) - 1) \tag{1}$$

The indicator was of no specific physical meaning and could simply be a very convenient tool for fault detection on a variety of scales. In this step, three indicator factors named F_i^1, F_i^2, and F_i^3 were obtained.

Thirdly, the minimum of the three was taken as the final enhancement result F_{all}:

$$F_{all} = \min(F_i^1, F_i^2, F_i^3) \tag{2}$$

This strategy could be concluded in the computational flow shown in Figure 1.

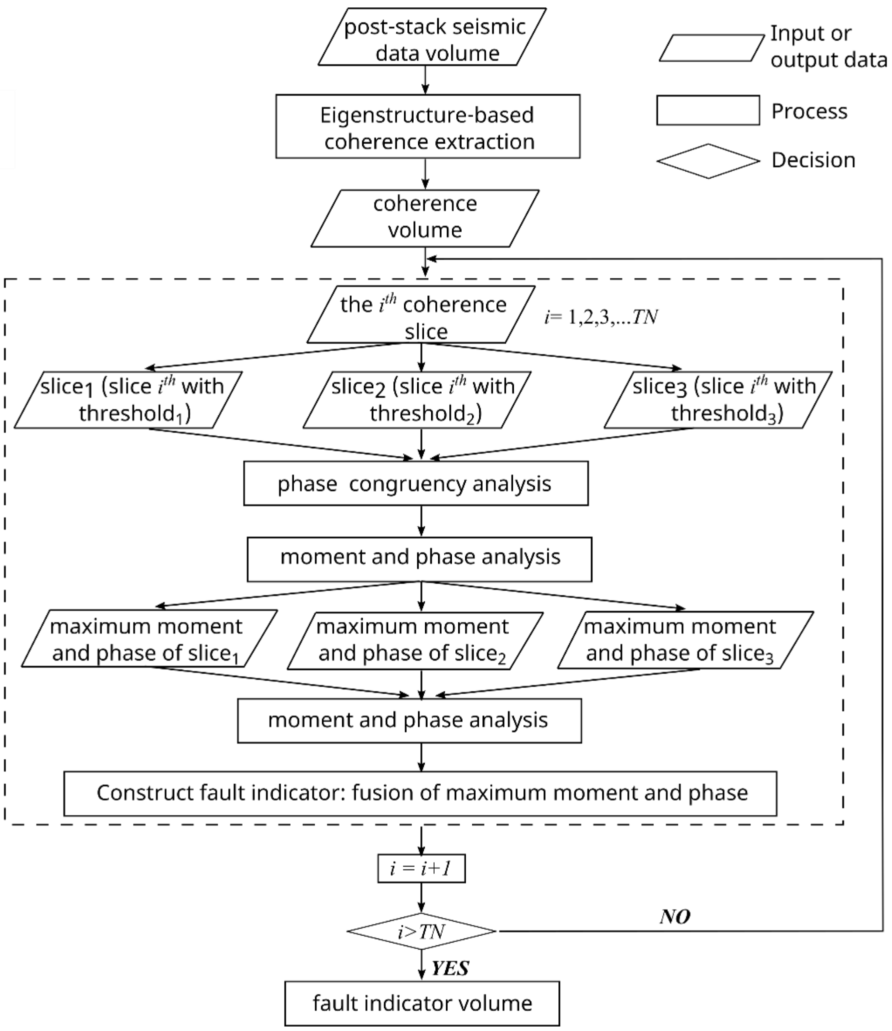

Figure 1. A flowchart illustrating the basic steps of this paper. *TN* denotes time slice number.

3. Model Test

A model of mesh size of 420 × 620 was designed based on the assumption of two joint faults with clearly displacement, called $fault_L$ and $fault_R$. There are secondary faults extending to the middle zone from them and eventually connecting. Two regions are focuses, one is the secondary fault $fault_S$ near the $fault_L$, and the other is the tiny fault development zone $fault_Z$ between $fault_L$ and $fault_R$. The coherence slice of this model (Figure 2a) shows us that $fault_S$ adjacent to $fault_L$ has some weak features, and tiny fault zone $fault_Z$ hardly has any visible fault features. Generally speaking, the fault zones should gradually decrease in size and displacement as they move away from primary faults [35]. As geophysicists have inferred, tiny faults may result in a small fluctuation in seismic data and weak difference in coherence. This leads to a mistake that main faults such as $fault_L$ and $fault_R$ appear as two completely isolated faults visually.

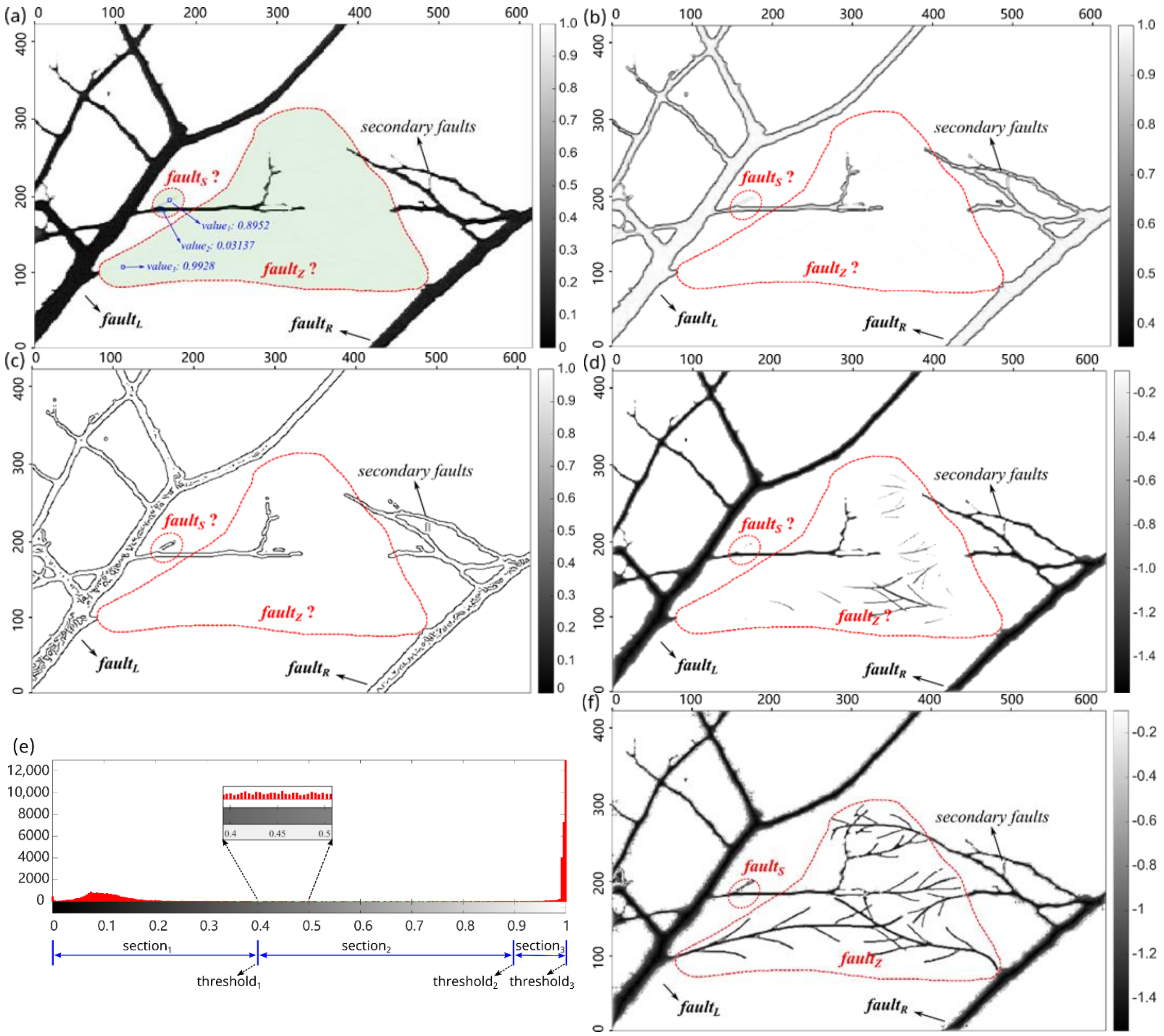

Figure 2. Comparison of coherence property slices (model data) of tiny faults (**a**) and their gradient properties (**b**), Canny boundaries (**c**), *PC* effects (**d**), the histogram of coherence and three-segment division (**e**), and *PC* results of segmented strategy and fusion (**f**). The single fault named $fault_S$ and the fault zone named $fault_Z$ (the green zone in the red dashed line) (shown in Figure 2a) are our main targets. The blue numbers in Figure 2a show the reader the values for the different fracture regions.

For the coherence of this model, the following three methods were applied to try to obtain a clearer distribution of both $fault_S$ and $fault_Z$.

(1) Extracting the gradient features of coherence by the following formula:

$$coh_{gradient} = \sqrt{coh_x^2 + coh_y^2} \tag{3}$$

where coh_x and coh_y are the directional derivatives of coherence in inline and crossline, respectively. The result of $coh_{gradient}$ is shown in Figure 2b.

(2) Extracting the discontinuity boundaries of coherence by the Canny operator, shown in Figure 2c.

(3) Extracting the discontinuity features of coherence by applying *PC* method directly, shown in Figure 2d.

(4) Presenting the histogram of coherence and using three-segment division, shown in Figure 2e.

(5) Extracting the discontinuity features of coherence by applying *PC* method of new strategy, shown in Figure 2f.

It is clear that the gradient of coherence, boundaries of Canny operator, and the direct *PC* attributes do not restore the targets, $fault_S$ and $fault_Z$, very well as shown in Figure 2. In b and c, the primary faults $fault_L$ and $fault_R$ were significantly highlighted, the secondary fault $fault_S$ can be identified to some extent but far from enough, and the fracture zone $fault_Z$ is not responsive at all. These phenomena are common for gradient-like methods. The direct application of *PC* is able to detect the complete primary faults, $fault_L$ and $fault_R$, only a few features of the secondary fault $fault_S$, and more detailed tiny faults in fracture zone $fault_Z$, shown in Figure 2d. There are three facts to be noted. First, the secondary fault $fault_S$ may be interfered by the adjacent primary fault $fault_L$ resulting in its incomplete features. Second, tiny faults near the primary and secondary faults are not effectively enhanced. There are hardly any fault-like features visible at the fringe of the fault zone $fault_Z$. Third, the tiny faults located in the central region of the fracture zone $fault_Z$, get more but inadequate enhancement. They are very far from the main faults.

The faults of different scales usually lie within different value ranges of the coherence. The histogram of the coherence (Figure 2a) is presented in Figure 2e. It can be roughly divided into 3 sections, where $section_1$ is [0,0.4], $section_2$ is [0.4,0.9], and $section_3$ is [0.9,1.0]. By the definition of coherence, it can be inferred that $section_1$ is the low value region and reveals the main faults. Section 2 is the medium value region and represents secondary faults. Section 3 is the high value region and depicts the homogeneous geological background and tiny faults. The three scattered values in Figure 2a show this phenomenon.

Figure 2f is the *PC* result of new segment extraction and fusion strategy. It shows great improvement in resolution in fault detection. The primary faults are well defined, while the features of secondary or crossed faults have been recovered very well. The morphology of our targets, $fault_S$ and $fault_Z$, are fully recovered. The two main faults, $fault_L$ and $fault_R$, can be joined together by secondary and tiny faults. Such results are clearly more convincing for studying reservoir connectivity than the initial coherence properties.

The above experiments demonstrate a weakness of the *PC* method and the key advantage of our new method. The close spatial distance and large difference in attribute values will lead to the mutual interference of primary faults, secondary faults, and tiny faults. Detailed analysis is as follows. The fault feature in coherence is an unsmooth non-periodic signal so that its fast Fourier transform (FFT) cannot fit the fault boundary perfectly. The unsmoothed fault boundary inevitably causes the so-called Gibbs effect [36]. It is known that the "ringing" noise around the discontinuities will generate when the image frequency band is truncated by a filter window and inverse-transformed to the time domain. Therefore, it is crucial to set the minimum scale wavelength when the Log–Gabor directional filter is adopted to involve the inverse fast Fourier transform (IFFT). When the minimum wavelength is large, the Log–Gabor filter with a large window of Gaussian function will continuously and slowly attenuate amplitude spectrum, and generate weak Gibbs effect at the discontinuous points of fault boundaries. After inverse transform, the image noise has large halos with weak amplitude and disperse energy. In this case, the noise can be effectively suppressed by simple threshold setting to obtain relatively clear and smoothed boundaries of primary faults. However, this operation may obtain unobservable tiny faults likely due to the smoothing effect of large window. In contrast, the filter with small minimum wavelength is so sensitive that it can detect tiny faults far away from the main faults. Meanwhile, the small Gaussian function window truncates the amplitude spectrum sharply and produces a strong Gibbs effect around the fault boundaries. This leads to severe interference in different-scale faults. As a result, the characteristics of tiny faults adjacent to the main faults are difficult to preserve even if the main faults can be identified by threshold setting. The new segmented and fusion strategy was proposed to solve this problem. We retained the fixed and optimized Gaussian filter parameters instead of just reducing the window, enhanced the discontinuities segment by segment, and made a suitable fusion. These operations avoided the strong Gibbs effect, reduced the impact of artificial noise, and finally restored the most fault-like features of the primary, secondary, and tiny faults. This will provide a better database for fault study.

4. Case Study

The Majiagou Formation, the object of this study, generally distributed in the central-eastern Ordos Basin, China, is in the survey X on the Yishan slope in the east of the central paleo-uplift of the basin (red frame box shown in Figure 3a). The Ordovician reservoirs in this area are mainly marine carbonate deposits, which are one of the major natural gas reservoirs in the basin. The precious analysis of present tectonics and ancient landform shows that the structure of the Majiagou Formation, controlled by the paleo-morphology at the bottom of the Ordovician System, has the characteristics of tectonic inheritance development. The Majiagou Formation is divided into six members from Ma1 to Ma6. The Ma2 member composed of mound-shoal dolomite is our target (shown in Figure 3b). The low amplitude tectonics are developed throughout the Ma2 member and the highest position is located in the central-eastern, with no regional large faults but tiny faults generally developed (shown in Figure 3c,d). Additionally, three eroded karst flutes are located in the northern, southern, and central parts of the work area, with pore caves and fractures.

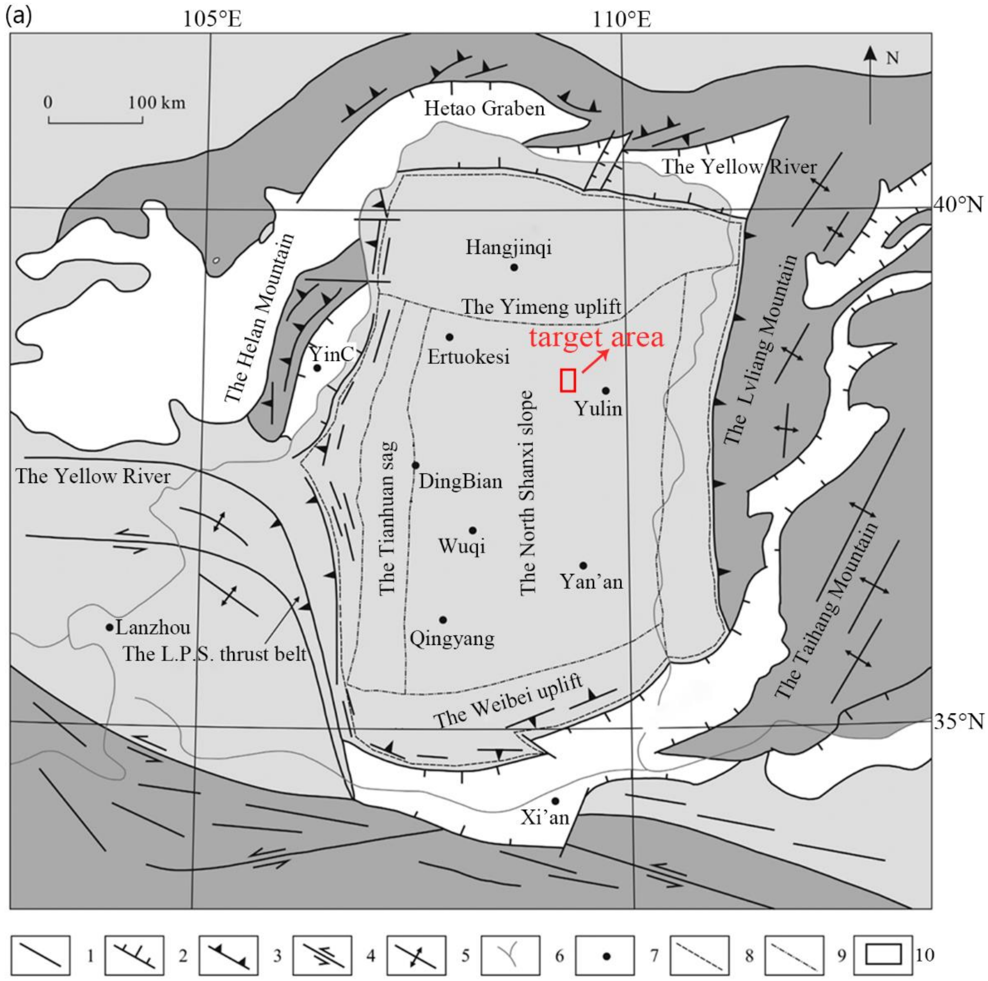

Figure 3. *Cont.*

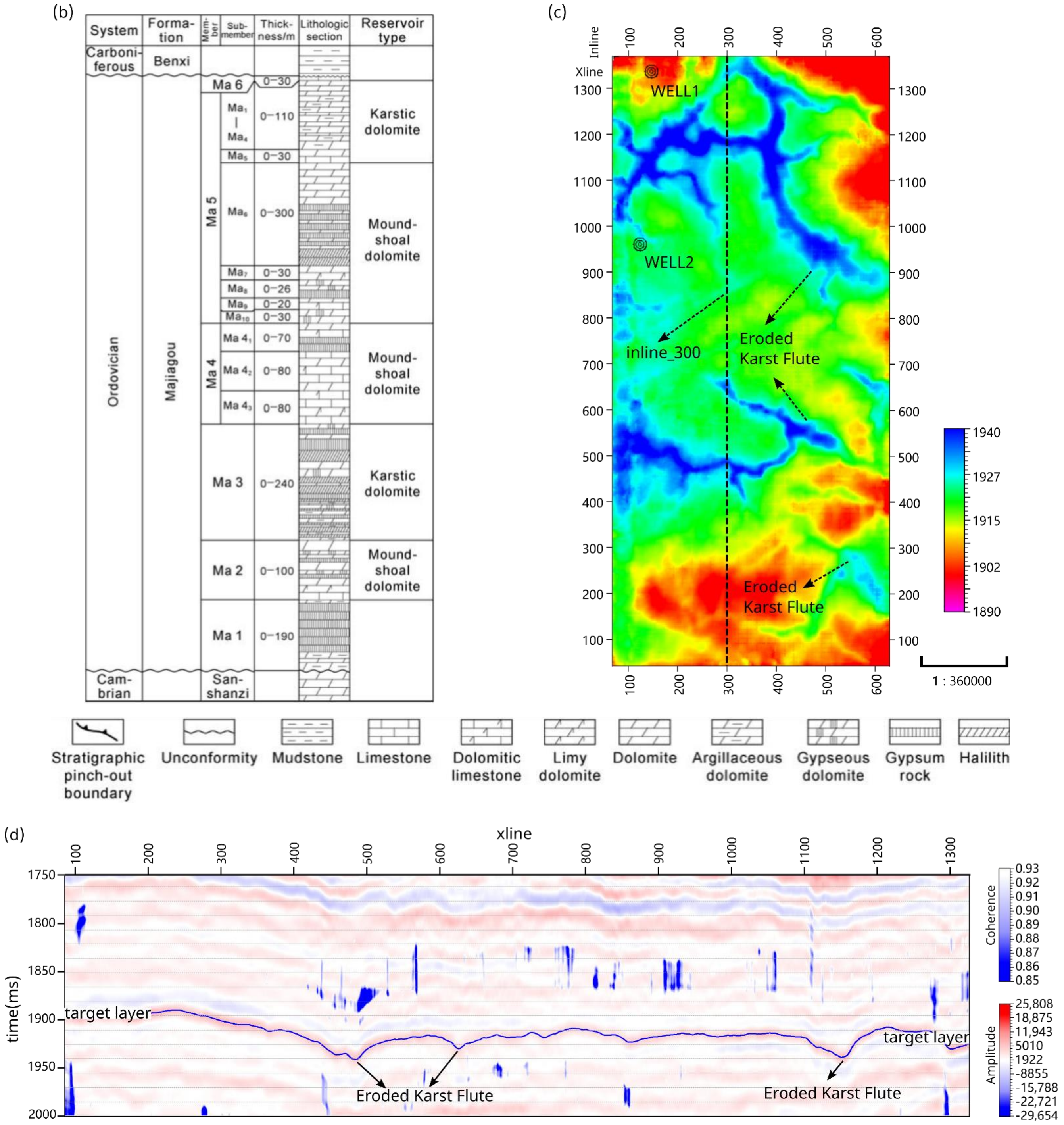

Figure 3. Target strata in the Majiagou Formation, Ordos Basin, China. (**a**) Tectonic framework and units of the basin (modified from reference [37]). The white area represents the young graben system around basin margins, and dark gray represents the deformation belts around the basin. 1. fault; 2. normal fault; 3. thrust fault; 4. strike-slip fault; 5. fold; 6. river; 7. city; 8. basin boundary; 9. tectonic unit boundary; 10. study area. (**b**) Comprehensive stratigraphic column of Ordovician Majiagou Formation obtained from previous studies [38]; (**c**) structure map of time domain for target layer; (**d**) profile of amplitude versus coherence for inline_300.

Figure 3 also shows the initial interpretation results of the target stratum, where Figure 3c is the structure map of time domain, Figure 3d is its amplitude and coherence of inline 300 (black-dashed line in Figure 3c). On the whole, our target stratum is located in a low-amplitude tectonics area with reflected time ranged from 1855 ms to 1938 ms. The eroded karst flutes are very distinguished in the structure map. The coherence presents some rough sketches of the three eroded karst flutes but cannot provide any details of tiny faults around them. Compared with the discontinuities in the base map, the fault features in the vertical profile are weaker (shown in Figure 3d). If we continue to intensify the thresholding, even if we may get some fault features near the flutes, we will end up with a blurry image. Next, typical property slices of the target layer were extracted for comparison and the improvement of the new method in fault detection is discussed.

The new method seems to have a significant improvement in lateral resolution and extension length of the faults. Figure 4 shows the attributes extracted from seismic data for Ma2 Member. They are (Figure 4a) the amplitude, (Figure 4b) coherence of third generation, (Figure 4c) dip, (Figure 4d) curvature, (Figure 4e) *PC* attribute, and (Figure 4f) *PC* attribute of new method. The coherence and dip present the main structure frameworks and nearly no details. There are large shaded areas near the boundaries of rivers and faults. The curvature provides very few small faults as expected. The results of *PC* and its new version show us clearer boundaries of main faults and tiny faults. They distinguished some features concealed in background and shaded areas, providing the possibility to identify more small faults. Three arbitrary lines (line 1, line 2, line 3) were selected for comparison of details in a closer way. In the coherence map (Figure 4b), fault-like features crossed by the three lines are hard to see. In the *PC* map (Figure 4e), these features crossed by line 2 and line 3 become clearer but the one crossed by line 1 remains blur. In the *PC* map of the new method (Figure 4f), fault-like features crossed by all lines are the clearest. Considering the extension and regularity, the likelihoods of these features being faults are very high.

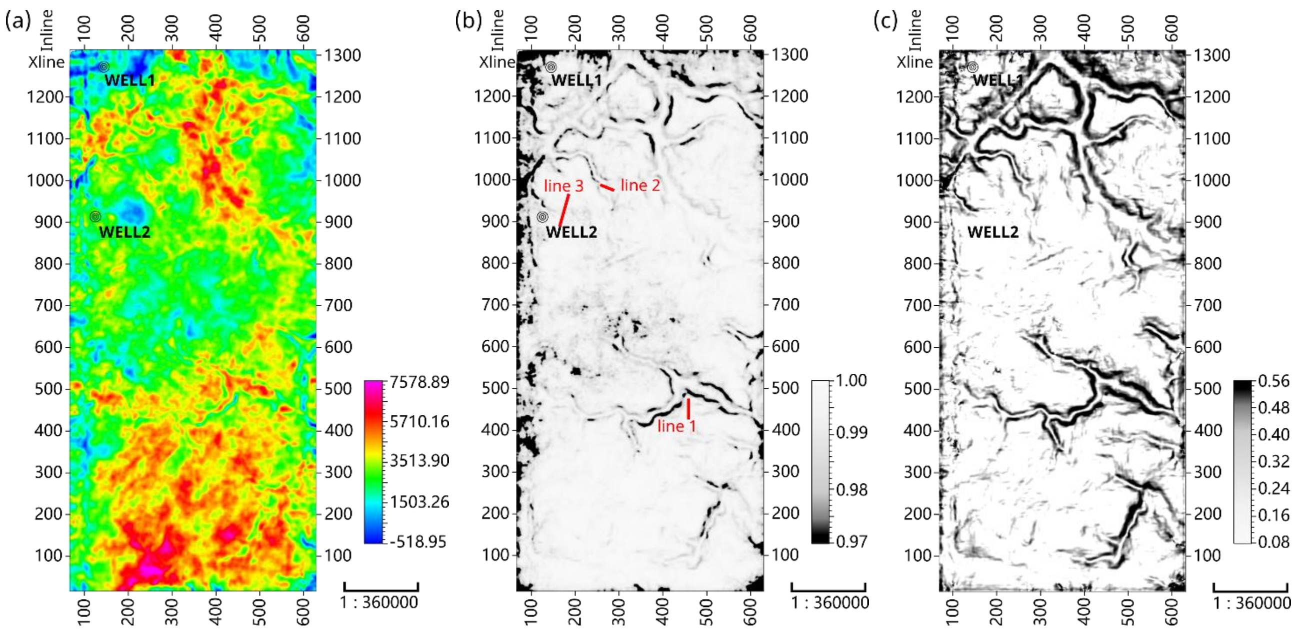

Figure 4. *Cont.*

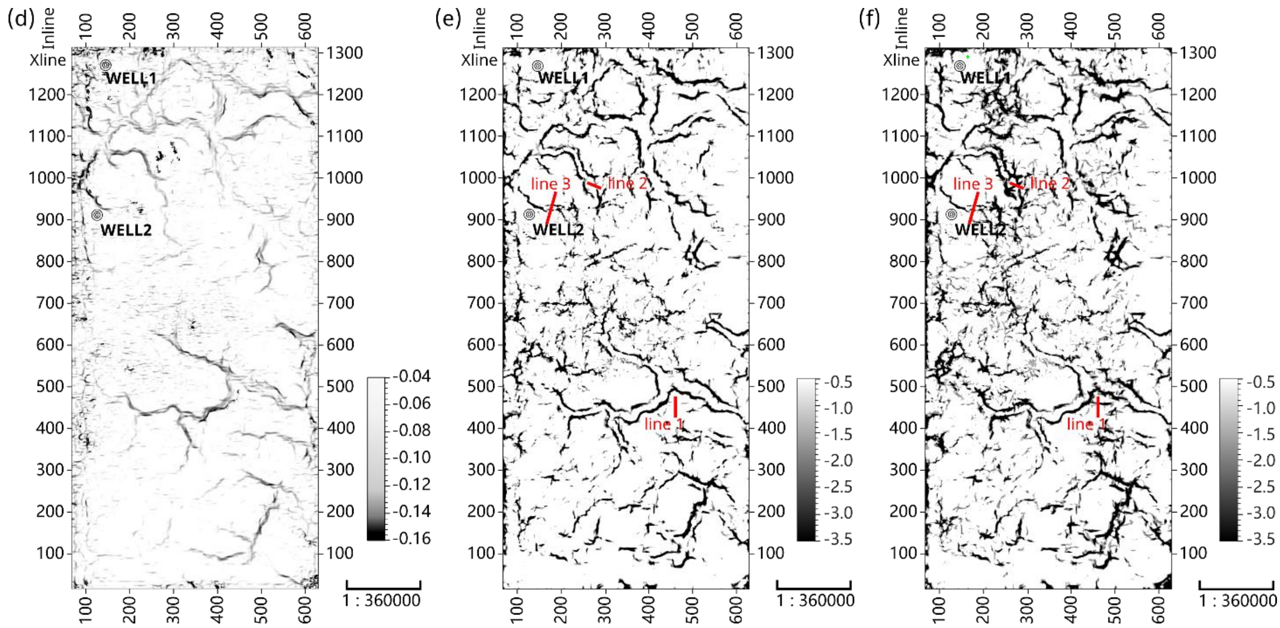

Figure 4. Comparison of fault detection results of the target layer. Line 1, line 2, and line 3 in red line are three arbitrary lines for further comparisons. (**a**) Amplitude, (**b**) coherence, (**c**) dip, (**d**) curvature, (**e**) *PC* attribute, (**f**) *PC* attribute (new method).

Next, some further comparisons were implemented in seismic profiles to verify the authenticity of these fault-like features (shown in Figures 5–7). The profiles of coherence, *PC* attribute, and the result of the new method in three arbitrary lines (line 1, line 2, and line 3) are extracted. They are displayed with amplitude in the same color-map scheme. For the three lines, the coherence, the results of *PC*, and the new method all present a similar pattern. The discontinuities gradually increase near the locations where the strata underwent weak undulations. Obviously, the new method reached the highest resolution. The hanging and foot wall of a fault are different in spatial location. When the fault displacement is large, the walls are expressed as travel time differences on the reflection seismic profile on both sides of the fault. When the displacement is small, the walls presented themselves as amplitude variation mainly. The undulation of the strata and the variation of the amplitude presented Figures 5a, 6a and 7a are weak but visible, and their enhanced results in (b) and (c) are reliable with high probabilities.

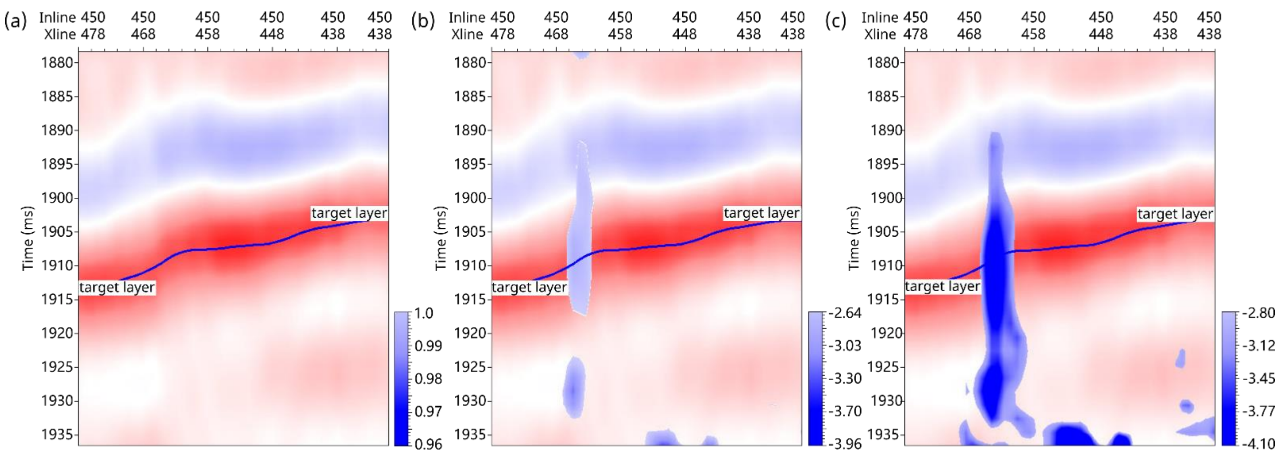

Figure 5. Different attributes crossed line 1. (**a**) Amplitude vs. coherence, (**b**) amplitude vs. *PC*, (**c**) amplitude vs. *PC* (new method).

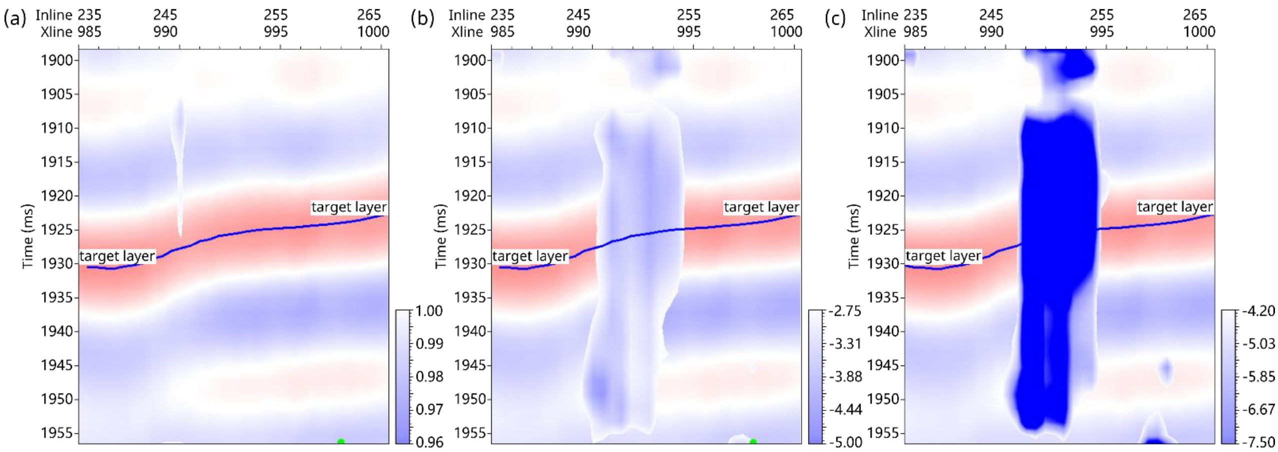

Figure 6. Different attributes crossed line 2. (**a**) Amplitude vs. coherence, (**b**) amplitude vs. *PC*, (**c**) amplitude vs. *PC* (new method).

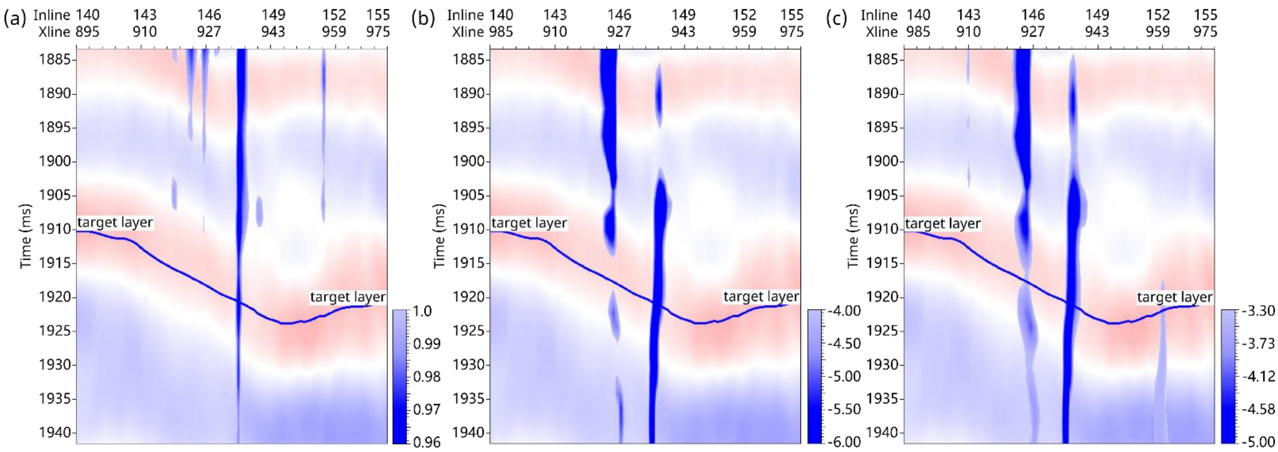

Figure 7. Different attributes crossed line 3. (**a**) Amplitude vs. coherence, (**b**) amplitude vs. *PC*, (**c**) amplitude vs. *PC* (new method).

Combining the fault-like features in both lateral and longitudinal directions, we have a high degree of confidence that such tiny faults are real.

5. Discussion

The advantages of the segmentation and fusion strategy proposed in this paper are significant. It inherits and reinforces the sensitivity of phase congruency method to tiny faults. Moreover, it mitigates the Gibbs effect in the filtering process. This weakens the disturbing effect of the main faults on the adjacent secondary and tiny faults, and greatly restores the fault features of different scales. It is very suitable for application in low-amplitude tectonic regions with lower noise level, such as the central region of Ordos Basin mentioned in this paper.

The strategy did not perform perfectly in the following cases. Firstly, it is inappropriate for areas affected by multi-period strong tectonic movements. For example, high and steep tectonic areas in the Tarim Basin and Qaidam Basin in China are not suitable. Strata in these areas tend to be severely fractured and have drastic lateral variations. Fault imaging accuracy is lower and structural noise is stronger. Some irregular anomalies in the coherence can interfere with the identification of normal breaks. Usually, we have to go by geological laws to get approximations. Secondly, the features of main and tiny faults extracted by our strategy are at almost the same level. This may bring some difficulties for the fault classification. This may be the unavoidable price we must pay for using normalized measures such as *PC*. If the decisive attributes of the fault displacement could be found in the future, it might be solved. Thirdly, the quality control of the segmentation of coherence depends on the experience of the interpreters. The faults of interest may be distributed over multiple value ranges, depending on the relationship of the adjacent seismic traces at the faults. The new method decreases the difficulties in manually setting reasonable thresholds but still not enough.

The authenticity of the enhanced fault-like features may be another focus of discussion. Generally, a fault can be determined to be true if the fault-like features of the profile and plane match. However, there are some cases that are difficult to detect. One of the most important aspects is fault shadow. Fault shadows are usually characterized by a number of secondary faults parallel to the main faults in coherence slices. For the interpreters, fault shadow phenomena caused by imperfect time-domain migration are difficult to capture and calibrate. This is the very challenge that is insurmountable by simple data-driven fault detection methods. Methods of image enhancement such as *PC* will strengthen these unexpected anomalies and confuse interpreters. In this regard, we can only hope that the pre-stack depth migration techniques could eliminate the structural artifacts. Another aspect is noise. Kovesi suggested that even a little noise may cause strong, fake image feature in phase congruency [22]. According to the noise characteristics of natural images, the de-noising technique was integrated in the *PC* method but does not apply to seismic attributes very well. Our strategy also did not achieve better results. For migrated seismic data obtained through a series of technical processes, no one knows what the real noise it contains should look like anymore. Setting a reasonable distribution of the noise response as a de-noising criterion based on the actual situation of the study area may yield better fault detection results.

In fact, the *PC* approach and its new version proposed in this paper did not make new faults, but simply normalized and amplified the hidden fault-like features in the coherence, and presented them better to the interpreter. This gave interpreters more evidence to confirm the existence of faults or not. That is what the strategy is all about. After all, a single approach cannot solve all the problems involved.

6. Conclusions

(1) The new segmented extraction and fusion strategy of the phase congruency were proposed and carried out to enhance tiny fault features successfully. This strategy mitigates the Gibbs effect of truncation window and decreases disturbances caused by main faults, and achieves higher resolution.

(2) The new strategy is applicable to low tectonic amplitude and gentle stratigraphy, and performs well in dense carbonate reservoirs in the Ordos Basin, China. Typical fault-like features were proved to be true by comparisons in both lateral and longitudinal directions.

(3) As a data-driven image enhancement method, this strategy cannot overcome all the problems in fault detection such as fault shadow and noises. Cooperation with other relevant geophysical techniques is necessary.

Author Contributions: E.W. conceived of the study idea, contributed theoretical ideas, designed the strategy, the work flow, and the model data, and wrote the code and the paper; H.L. provided his practical experience and discussed the results; R.H. translated the paper; W.Z. provided migrated seismic data and geological background information; L.L. contributed efforts to the 3D version; C.X. and G.Y. discussed in the model data; Q.C. and Q.Y. conducted some real data tests. All authors have read and agreed to the published version of the manuscript.

Funding: This research was funded by the key technology research project of China National Petroleum Corporation (grant number: 2021ZG03) and scientific research and technology development projects of China National Petroleum Corporation (grant number: 2021DJ3701).

Data Availability Statement: The model data were obtained from public image data on the Internet, and the field data are confidential.

Conflicts of Interest: The authors declare no conflict of interest.

Appendix A

The core theoretical formula of two-dimensional *PC* proposed by Kovesi [18] is:

$$PC_{2D}(x_1, x_2) = \frac{\sum_o \sum_s W(x_1, x_2) \lfloor A_{os}(x_1, x_2) \Delta\phi_{os}(x_1, x_2) - T \rfloor}{\sum_o \sum_s A_{os}(x_1, x_2) + \varepsilon} \tag{A1}$$

$$\Delta\phi_{os}(x_1, x_2) = \cos\left[\phi_{os}(x_1, x_2) - \overline{\phi}(x_1, x_2)\right] - \left|\sin\left[\phi_{os}(x_1, x_2) - \overline{\phi}(x_1, x_2)\right]\right| \tag{A2}$$

where a point of interest for an image $PC_{2D}(x_1, x_2)$ is the *PC* value at the point (x_1, x_2), which is a dimensionless variable from 0 to 1, meaning that the image features change from weakness to strength; $W(x_1, x_2)$ is the weight function of frequency distribution; s and o are the scale and direction of log–Gabor filter, respectively, $A_{os}(x_1, x_2)$ is the amplitude at the scale s and direction o; $\phi_{os}(x_1, x_2)$ is the local phase angle; $\overline{\phi}(x_1, x_2)$ is the amplitude weighted mean local phase angle; T is noise compensation factor; ε is a small constant to prevent the denominator from being 0; $\lfloor\rfloor$ indicates that the value inside the symbol is taken as itself when positive, otherwise it is taken as 0.

After obtaining the *PC* attribute, moment analysis is carried out. There are two most important variables, maximum moment and minimum moment. The maximum moment M represents image edge; the minimum moment m represents image corner. The respective formulae are as follows:

$$M = 1/2\left(c + a + \sqrt{b^2 + (a-c)^2}\right) \tag{A3}$$

$$m = 1/2\left(c + a - \sqrt{b^2 + (a-c)^2}\right) \tag{A4}$$

where

$$a = \sum_o (PC(o)\cos(o))^2 \tag{A5}$$

$$b = 2\sum_o (PC(o)\cos(o)) \times (PC(o)\sin(o)) \tag{A6}$$

$$c = \sum_o (PC(o)\sin(o))^2 \tag{A7}$$

Another crucial concept is the amplitude-weighted mean local phase angle $\overline{\phi}$. The respective formula is as follows:

$$\overline{\phi} = \arctan(E_{real}, E_{imag}) \tag{A8}$$

where arctan is the arctangent operator represented by radians; E_{real} and E_{imag} denote the energies of real and imaginary part of the inverse-transformed image. They could be obtained by the following formula:

$$I_T = \mathrm{IFFT}(\mathrm{FFT}(I) \times F_{\log-gabor}) \tag{A9}$$

$$E_{real} = \sum_o \sum_s \mathrm{Real}(I_T) \tag{A10}$$

$$E_{imag} = \sqrt{\left(\sum_o \sum_s \mathrm{Imag}(I_T)\cos(o)\right)^2 + \left(\sum_o \sum_s \mathrm{Imag}(I_T)\sin(o)\right)^2} \tag{A11}$$

where I denotes the original image, I_T denotes its result after 2D-inversed FFT, $F_{\log-gabor}$ is two-dimensional log–Gabor spectrum, and Real and Imag are the real and imaginary operators of complex numbers, respectively.

References

1. Jia, C. Breakthrough and significance of unconventional oil and gas to classical petroleum geology theory. *Pet. Explor. Dev.* **2017**, *44*, 1–10. [CrossRef]
2. Zou, C.; Yang, Z.; He, D.; Wei, Y.; Li, J.; Jia, A.; Chen, J.; Zhao, Q.; Li, Y.; Li, J.; et al. Theory, technology and prospects of conventional and unconventional natural gas. *Pet. Explor. Dev.* **2018**, *45*, 604–618. [CrossRef]
3. Jiao, F. Re-recognition of "unconventional" in unconventional oil and gas. *Pet. Explor. Dev.* **2019**, *46*, 847–855. [CrossRef]
4. Song, Y.; Li, Z.; Jiang, Z.; Luo, Q.; Liu, D.; Gao, Z. Progress and development trend of unconventional oil and gas geological research. *Pet. Explor. Dev.* **2017**, *44*, 675–685. [CrossRef]
5. Thai Ba, N.; Vo Thanh, H.; Sugai, Y.; Sasaki, K.; Nguele, R.; Phi Hoang Quang, T.; Luong Bao, M.; Le Nguyen Hai, N. Applying the hydrodynamic model to optimize the production for crystalline basement reservoir, X field, Cuu Long Basin, Vietnam. *J. Pet. Explor. Prod. Technol.* **2020**, *10*, 31–46. [CrossRef]
6. Dempsey, E.D.; Holdsworth, R.E.; Di Toro, G. The Role of Reactivation and Fluid Pressure Cycling in The Development of Late Zeolite-bearing Faults and Fractures From The Adamello Batholith, Italy. *AGU Fall Meet. Abstr.* **2011**, *2011*, T31C-2361.
7. Missenard, Y.; Rocher, M.; Vergely, P.; Casteleyn, L.; Robion, P.; Cushing, M.E.; Bertrand, A.; Benedicto, A. Differential Fracturing Pattern in Clay/limestone Alternations and Fluid Circulations in the Maltese Islands. In Proceedings of the 2nd International Conference on Fault and Top Seals—From Pore to Basin Scale; European Association of Geoscientists & Engineers: Montpellier, France, 21–24 September, 2009; p. 16. [CrossRef]
8. Du, W.F.; Peng, S.P.; Shi, S.Z.; Cui, X.Q. Buried Structure 3D Seismic Interpretation of Coal Mining District and Its Safety Influence on Coal Mine. *Eur. Assoc. Geosci. Eng.* **2017**, *2017*, 1–5. [CrossRef]
9. Lin, J.; Zuo, Y.; Zhang, K.; Sun, W.; Jin, B.; Li, T.; Chen, Q.-G. Coal and Gas Outburst Affected by Law of Small Fault Instability during Working Face Advance. *Geofluids* **2020**, *2020*, 8880091. [CrossRef]
10. Ren, H.S.; Lu, S.F.; Xiao, D.S. Interpretation Methods and Application of Small Faults. *Adv. Mater. Res.* **2014**, *962–965*, 132–137. [CrossRef]
11. Sun, S.G.; Feng, S.J.; Lei, J.H. Water-Inrush Mechanism while Fault Zone Secondary Activated in Mining. *Adv. Mater. Res.* **2012**, *524–527*, 799–802. [CrossRef]
12. Wang, Y.; Jiang, Y.; Zhang, X.; Li, C.; Piao, C. Characterization Application of 3D seismic interpreting technique in the oilfield development under the condition of dense well pattern. In Proceedings of the Beijing 2014 International Geophysical Conference & Exposition, Beijing, China, 21–24 April 2014; pp. 1020–1023. [CrossRef]
13. Wang, H.; Liu, T. Enhancing estimation of drop height for small scale faults by sampling. *Coal Geol. Explor.* **2000**, *28*, 59–61.
14. Xuelei, F.; Fengshan, M.; Haijun, Z.; Jie, G. Numerical simulation of hydraulic fracturing in shale gas reservoirs under fault influence. *J. Eng. Geol.* **2021**, *29*, 751–763. [CrossRef]
15. Yang, Y.; Zoback, M.D. The role of preexisting fractures and faults during multistage hydraulic fracturing in the Bakken Formation. *Interpretation* **2014**, *2*, SG25–SG39. [CrossRef]
16. Kozłowska, M.; Brudzinski, M.R.; Friberg, P.; Skoumal, R.J.; Baxter, N.D.; Currie, B.S. Maturity of nearby faults influences seismic hazard from hydraulic fracturing. *Proc. Natl. Acad. Sci. USA* **2018**, *115*, E1720–E1729. [CrossRef]
17. Vo Thanh, H.; Sugai, Y.; Nguele, R.; Sasaki, K. Integrated workflow in 3D geological model construction for evaluation of CO_2 storage capacity of a fractured basement reservoir in Cuu Long Basin, Vietnam. *Int. J. Greenh. Gas Control.* **2019**, *90*, 102826. [CrossRef]
18. Gersztenkorn, A.; Marfurt, K.J. Eigenstructure-based coherence computations as an aid to 3-D structural and stratigraphic mapping. *Geophysics* **1999**, *64*, 1468–1479. [CrossRef]
19. Randen, T.; Pedersen, S.I.; Sønneland, L. Automatic extraction of fault surfaces from three-dimensional seismic data. In *Seg Technical Program Expanded Abstracts 2001*; Society of Exploration Geophysicists: San Antonio, TX, USA, 2001; pp. 551–554. [CrossRef]
20. Roberts, A. Curvature attributes and their application to 3D interpreted horizons. *First Break* **2001**, *19*, 85–100. [CrossRef]
21. Hale, D. Structure-oriented smoothing and semblance. *CWP Rep.* **2009**, *635*, 261–270.
22. Kovesi, P. Image features from phase congruency. *Videre J. Comput. Vis. Res.* **1999**, *1*, 1–26.
23. Chien, Y. Pattern classification and scene analysis. *IEEE Trans. Autom. Control* **1974**, *19*, 462–463. [CrossRef]
24. Marr, D.; Hildreth, E.; Brenner, S. Theory of edge detection. *Proc. R. Soc. Lond. Ser. B Contain. Pap. A Biol. Character. R. Soc.* **1980**, *207*, 187–217. [CrossRef]
25. Canny, J. A Computational Approach to Edge Detection. *IEEE Trans. Pattern Anal. Mach. Intell.* **1986**, *8*, 679–698. [CrossRef]
26. Kovesi, P. Phase Congruency Detects Corners and Edges. In Proceedings of the the International Conference on Digital Image Computing: Techniques and Applications, DICTA 2003, Macquarie University, Sydney, Australia, 10–12 December 2003; pp. 309–318.
27. Kovesi, P. Phase congruency: A low-level image invariant. *Psychol. Res.* **2000**, *64*, 136–148. [CrossRef]
28. Kovesi, P.; Department, P.K. Edges Are Not Just Steps. In Proceedings of the ACCV2002: The 5th Asian Conference on Computer Vision, Melbourne, Australia, 23–25 January 2002.
29. Russell, B.; Hampson, D.; Logel, J. Applying the phase congruency algorithm to seismic data slices: A carbonate case study. *First Break* **2010**, *28*, 83–90. [CrossRef]

30. Shafiq, A.; Alaudah, Y.; Di, H.; Alregib, G. Salt Dome Detection within Migrated Seismic Volumes Using Phase Congruency. *SEG Tech. Program Expand. Abstr.* **2017**, 2360–2365. [CrossRef]
31. Karbalaali, H.; Javaherian, A.; Dahlke, S.; Torabi, S. Channel edge detection using 2D complex shearlet transform: A case study from the South Caspian Sea. *Explor. Geophys.* **2018**, *49*, 704–712. [CrossRef]
32. Kovesi, P.; Richardson, B.; Holden, E.-J.; Shragge, J. Phase-Based Image Analysis of 3D Seismic Data. *ASEG Ext. Abstr.* **2012**, *2012*, 1–4. [CrossRef]
33. Liao, L. Fracture and Fault Detection Based on Seismic Coherence Data. Master's Thesis, University of Electronic Science and Technology of China, Chengdu, China, 2020.
34. Wang, E.; Zhang, J.; Yan, G.; Yang, Q.; Zhao, W.; Xie, C.; He, R. Concealed-Fault Detection in Low-Amplitude Tectonic Area—An Example of Tight Sandstone Reservoirs. *Minerals* **2021**, *11*, 1122. [CrossRef]
35. Mitchell, T.M.; Faulkner, D.R. The nature and origin of off-fault damage surrounding strike-slip fault zones with a wide range of displacements: A field study from the Atacama fault system, northern Chile. *J. Struct. Geol.* **2009**, *31*, 802–816. [CrossRef]
36. Lichman, E.; Northwood, E.J. High-resolution velocity notch filter without Gibbs effect. *Geophysics* **1997**, *62*, 274–287. [CrossRef]
37. Wang, J.; Ju, W.; Shen, J.; Sun, W. Quantitative prediction of tectonic fracture distribution in the Chang 7-1 reservoirs of the Yanchang Formation in the Dingbian area, Ordos basin. *Geol. Explor.* **2016**, *52*, 966–973.
38. Zhou, J.; Yu, Z.; Wu, D.; Ren, J.; Zhang, D.; Wang, S.; Yin, C.; Liu, Y. Restoration of formation processes of dolomite reservoirs based on laser U-Pb dating: A case study of Ordovician Majiagou Formation, Ordos Basin, NW China. *Pet. Explor. Dev.* **2022**, *49*, 327–338. [CrossRef]